Atmos. Meas. Tech. Discuss., 3, 2681–2721, 2010
www.atmos-meas-tech-discuss.net/3/2681/2010/
doi:10.5194/amtd-3-2681-2010

Atmospheric Measurement Techniques Discussions

Inherent calibration of a novel LED-CE-DOAS instrument to measure iodine oxide, glyoxal, methyl glyoxal, nitrogen dioxide, water vapour and aerosol extinction in open cavity mode

R. Thalman[1] **and R. Volkamer**[1,2]

[1]Department of Chemistry and Biochemistry, University of Colorado, Boulder, CO 80309, USA
[2]Cooperative Institute for Research in the Environmental Sciences CIRES, Boulder, CO 80309, USA

Received: 1 May 2010 – Accepted: 1 June 2010 – Published: 24 June 2010

Correspondence to: R. Volkamer (rainer.volkamer@colorado.edu)

Published by Copernicus Publications on behalf of the European Geosciences Union.

Abstract

The combination of Cavity Enhanced Absorption Spectroscopy (CEAS) with broad-band light sources (e.g. Light-Emitting Diodes, LEDs) lends itself to the application of cavity enhanced Differential Optical Absorption Spectroscopy (CE-DOAS) to perform sensitive and selective point measurements of multiple trace gases and aerosol extinction with a single instrument. In contrast to other broad-band CEAS techniques, CE-DOAS relies only on the measurement of relative intensity changes, i.e. does not require knowledge of the light intensity in the absence of trace gases and aerosols (I_0). We have built a prototype LED-CE-DOAS instrument in the blue spectral range (420–490 nm) to measure nitrogen dioxide (NO_2), glyoxal (CHOCHO), methyl glyoxal (CH_3COCHO), iodine oxide (IO), water vapour (H_2O) and oxygen dimers (O_4). We demonstrate the first CEAS detection of methyl glyoxal, and the first CE-DOAS detection of CHOCHO and IO. A further innovation consists in the measurement of extinction losses from the cavity, e.g. due to aerosols, at two wavelengths by observing O_4 (477 nm) and H_2O (443 nm) and measuring the pressure, relative humidity and temperature independently. This approach is demonstrated by experiments where laboratory aerosols of known size and refractive index were generated and their extinction measured. The measured extinctions were then compared to the theoretical extinctions calculated using Mie theory ($3–7\times10^{-7}$ cm^{-1}). Excellent agreement is found from both the O_4 and H_2O retrievals. This enables the first inherently calibrated CEAS measurement in open cavity mode (mirrors facing the open atmosphere), and eliminates the need for sampling lines to supply air to the cavity, and/or keep the cavity enclosed and aerosol free. Measurements in open cavity mode are demonstrated for CHOCHO, CH_3COCHO, NO_2, H_2O and aerosol extinction at 477 nm and 443 nm. Our prototype LED-CE-DOAS provides a low cost, yet research grade innovative instrument for applications in simulation chambers and in the open atmosphere.

AMTD
3, 2681–2721, 2010

1 Introduction

Light-Emitting Diode (LED) light sources coupled with Cavity Enhanced Absorption Spectroscopy (CEAS) and Differential Optical Absorption Spectroscopy (DOAS) retrievals hold great potential for a light-weight, low-power and portable instrument to enable the sensitive and selective measurement of numerous atmospheric trace gases and aerosol extinction with a single instrument. In the last ten years several high-finesse cavity techniques have expanded on the principles of Cavity Ring-Down Spectroscopy (CRDS) (Okeefe and Deacon, 1988; Brown, 2003). CRDS, CEAS, and integrated cavity output spectroscopy (ICOS) have in common the use of a high–finesse optical cavity consisting of two highly reflective mirrors to increase the absorption path length over that of conventional White-type (White, 1942) or Harriet-type (Herriott and Schulte, 1965) multi-reflection cells by several orders of magnitude (factor 100–1000). The long path length leads to greatly increased sensitivities of these techniques. CEAS works on many of the same principles as CRDS, but can be coupled with broad band (non-laser) light sources, either in the form of thermal emitters (Incoherent Broadband CEAS) or LEDs (LED-CEAS). CEAS techniques have been used to measure a wide variety of atmospheric trace gases including nitrogen dioxide (NO_2) (Ball et al., 2004; Venables et al., 2006; Langridge et al., 2006, 2008a, b; Gherman et al., 2008; Triki et al., 2008; Washenfelder et al., 2008; Wu et al., 2009), the nitrate radical (NO_3)(Ball et al., 2004; Venables et al., 2006; Langridge et al., 2006, 2008a, b; Gherman et al., 2008; Meinen et al., 2008; Triki et al., 2008; Schuster et al., 2009), dinitrogen pentoxide (N_2O_5) (Schuster et al., 2009), nitrous acid (HONO) (Gherman et al., 2008), water vapor (H_2O) (Venables et al., 2006; Langridge et al., 2008a, b; Washenfelder et al., 2008), ozone (O_3) (Venables et al., 2006), oxygen dimer (O_4) (Langridge et al., 2006), iodine (I_2) (Ball et al., 2004; Vaughan et al., 2008; Dixneuf et al., 2009), iodine monoxide (IO) (Vaughan et al., 2008), iodine dioxide (OIO) (Vaughan et al., 2008), and glyoxal (CHOCHO) (Washenfelder et al., 2008). CEAS techniques that have been used to measure atmospheric trace gases in the blue spectral range (420–490 nm) are shown in Table 1.

AMTD
3, 2681–2721, 2010

These techniques have incorporated both Xe-arc lamps and LEDs as light sources.

Traditional CEAS techniques rely on absolute intensity measurements to determine trace gas extinctions (Fiedler et al., 2003). Such measurements are susceptible to lamp drifts. Additionally, all currently existing CEAS instruments suffer from the need to separate and quantify the temporal variability of extinction losses due to aerosols from that caused by trace gases. CEAS measurements to date require separate calibration measurements to characterize the temporal variability of aerosol extinction in the atmosphere, or require the removal of aerosols from the cavity by means of filtration in sampling lines. Cavity Enhanced Differential Optical Absorption Spectroscopy (CE-DOAS) is a novel CEAS technique under development (Meinen et al., 2008; Platt et al., 2009). CE-DOAS in principle holds promise to decouple aerosol and trace gas extinction, but this potential had as of yet not been developed. CE-DOAS and other CEAS techniques have in common the use of a high finesse optical cavity coupled to a broad band light source; broad areas of the spectrum are simultaneously measured by means of a single detector (multiplexing advantage). DOAS retrievals are inherently insensitive to variations in the absolute light intensity (Platt and Stutz, 2008), as DOAS relies on measuring narrow band (<3–5 nm FWHM) "differential" absorption features of trace gases; the differential absorption is independent of intensity variations, i.e., does not require knowledge of the light intensity in the absence of absorbers, I_0. In particular, lamp drifts or the presence of aerosols, both broadband extinction processes, do not affect the fitting of narrow band structures, which a DOAS retrieval separates from broad band extinction by means of numerical high-pass filtering of the spectra. First attempts have coupled CEAS hardware with a DOAS retrieval algorithm (Meinen et al., 2008), and discussed the peculiarities of differential retrievals in optical cavities (Platt et al., 2009). Platt et al. (2009) showed that the average (1/e) path length in the cavity is given by the following equation:

$$\bar{L} = \frac{d_0}{1 - R(\lambda) + \varepsilon_{\mathrm{Ray}}(\lambda) d_0 + \varepsilon_{\mathrm{Mie}}(\lambda) d_0 + \Sigma \sigma_i c_i d_0} \quad (1)$$

AMTD
3, 2681–2721, 2010

where d_0 is the cavity length, R is the mirror reflectivity, ε_{Ray}, is the extinction due to Rayleigh scattering, ε_{Mie} is the extinction due to aerosols and σ is the absorption cross-section of a trace absorber. The various extinction processes (denominator of Eq. 1) contribute to the reduction in path length; however past CE-DOAS configurations did not have the means to quantitatively account for the reduction in path length caused by temporally variable aerosol extinction. The strong sensitivity of Eq. (1) towards aerosol extinction is illustrated in Fig. 1, where the individual extinction losses are shown for our cavity. As the extinction loss increases, the effective path length decreases. Aerosols are highly variable in the atmosphere, and as a result the effective path length becomes time dependent. Furthermore, the different contributions to the overall extinction have different wavelength dependencies. The effective wavelength dependent path length is thus no longer determined exclusively by R, and α_{Ray}, and their known wavelength dependencies. In the presence of aerosols, wavelength dependence in Eq. (1) is no longer well defined. Past attempts to characterize broad band extinction losses by means of separate extinction calibration measurements have mostly been limited to the characterization of mirror reflectivity by the use of O_4 (446 nm band with enriched oxygen content) (Langridge et al., 2006), NO_2 (using a known NO_2 mixture) (Langridge et al., 2006; Venables et al., 2006; Gherman et al., 2008; Triki et al., 2008; Vaughan et al., 2008) or CO_2 (Orphal and Ruth, 2008); a similar approach was applied to aerosols by (Varma et al., 2009) using the O_2 band at 685nm in the SAPHIR chamber. An inherent means to calibrate path length as a function of wavelength under atmospheric conditions in the presence of variable atmospheric turbulence and aerosols is desirable, and are currently missing.

The blue spectral range holds great potential to detect multiple interesting molecules directly in the atmosphere. Glyoxal is the smallest alpha-dicarbonyl and a novel indicator species for fast photochemistry of volatile organic compounds (VOCs) on local (Volkamer et al., 2005b; Sinreich et al., 2007) and global scales (Kurosu et al., 2005; Wittrock et al., 2006; Vrekoussis et al., 2009). The global CHOCHO source from land ranges between 50 and 108 $Tg\,yr^{-1}$, with a single VOC precursor, isoprene,

AMTD
3, 2681–2721, 2010

contributing ca. 30% to the currently known sources (Myriokefalitakis et al., 2008; Fu et al., 2008; Stavrakou et al., 2009), but about half of the terrestrial source is currently unaccounted for (Stavrakou et al., 2009). Recent measurements demonstrate the uncertainties in the amount of glyoxal formed from isoprene. Current isoprene oxidation schemes consider glyoxal to be only a second and higher generation oxidation product (Bloss et al., 2005; Taraborrelli et al., 2009), but recent measurements (Volkamer et al., 2005a) confirm theoretical predictions (Dibble, 2004a; Dibble, 2004b), and demonstrate that it is also formed as a first generation product with a yield of up to 3% (Volkamer et al., 2005a). This corresponds to about an additional 10 Tg/yr of a glyoxal source on global scales that is currently not reflected in atmospheric models. While significant, it does not explain all of the missing glyoxal in biogenic areas. Further, there is also consistent evidence that CHOCHO is a building block for secondary organic aerosol (SOA) formation (Jang et al., 2002; Hastings et al., 2005; Liggio et al., 2005; Volkamer et al., 2007, 2009; Galloway et al., 2009). SOA is a concern for public health (Villalobos-Pietrini et al., 2007) and elevated SOA is linked to increased mortality rates (Pope and Dockery, 2006).Experimental in situ techniques that are sensitive enough to measure CHOCHO directly in the open atmosphere with good time resolution are only recently becoming available (Huisman et al., 2008; Washenfelder et al., 2008), and hold great potential to advance our scientific understanding of hydrocarbon and SOA sources on local and global scales.

The blue spectral range is particularly attractive, as multiple gases with potential climate relevance are accessible here, e.g., IO and CHOCHO (Volkamer et al., 2010). A typical light source for these instruments is the Xe-arc lamp; however, the use of Xe-arc lamps creates complications in CEAS retrievals, see Fig. 2 in Washenfelder et al. (2008), because Xe-gas emission lines overlap here with the spectral structures of glyoxal and other gases. The spectral intensity and shape of these lines depends on temperature and pressure of the Xe gas, which fluctuate over time. The resulting temporal variability of the Xe-gas emission lines complicates DOAS applications of Xe-arc lamps in this spectral range. As the number of commercially available high-powered

AMTD
3, 2681–2721, 2010

LEDs has increased, LEDs are starting to provide an interesting alternative light source to Xe-arc lamps to make the blue spectral range more accessible. Here we present an innovative prototype instrument that actively addresses all of these challenges, and enables the first well calibrated CEAS measurement of trace gases and aerosol extinction by a single measurement in open cavity mode under atmospheric conditions.

2 Experimental

2.1 Description of LED-CE-DOAS Instrument

Figure 2 depicts the set up of the LED-CE-DOAS instrument. Light from the LED is collimated and directed into the optical cavity where it makes many passes through the sample volume and is then focused onto the optical fiber and detected by the spectrometer/detector system attached.

2.1.1 Characterization of LED light sources

The criteria for a suitable blue LED for LED-CE-DOAS are: (1) lack of a Fabry-Pérot etalon; (2) match well with the expected reflectivity of the mirrors (Fig. 3a); (3) high light output, and (4) reasonably small chip size (<1 mm^2). Variations of etalon structures, which are periodic emission features arising from the difference in the refractive indices of the coating layers on the LED chip, are caused by fluctuations in either the current (amperage) or the temperature of the LED chip, and can complicate the elimination of spectral features from the LED emission spectrum thus introducing residual structures that limit the sensitivity of the DOAS approach. While the presence of etalon structures does not present a fundamental limitation (it can be eliminated by temperature stabilizing the LED, viewing the LED at an angle and using an extra stable power supply) (Kern et al., 2006; Sihler et al., 2009), the absence of etalon structures is desirable.

A variety of LEDs were tested. The LED emission spectrum and its spectral stability were characterized both as a function of electrical power and of time. The optical power

AMTD
3, 2681–2721, 2010

output was measured using an optical power meter (Thorlabs, PM210) (Table 2). The Seoul and LEDengin blue LEDs matched best with the mirror reflectivity, did not show etalon structure, and had an optimal emission pattern for the application. In absolute intensity the LEDengin LED was found to be the most powerful LED. In Fig. 3a the measured optical output from the various LEDs are compared to that calculated for a 450W Xe-arc lamp. At the peak of the LED emission spectrum the LED is found to be more powerful than the arc lamp. Due to the combination of advantages, we chose the LEDengin for our LED-CE-DOAS light source. The LED was mounted to a temperature controlled cooling stage, which was PID stabilized at 10±0.1 °C, to control variability in the LED output and structure (peak width and dominant wavelength) that vary with the current and temperature.

2.1.2 Characterization of the optical cavity and mirror reflectivity

The optical cavity (Fig. 2) consists of two 2.5 cm mirrors with a one meter radius of curvature and a reflectivity of 99.996% (Advanced Thin Films- Boulder, CO), which are mounted 99.0 cm apart. Out of band light was removed using a colored glass filter (Schott GG420) before the cavity and a band-pass filter (Newport 10BPF70-450, λ=450 nm, FWHM=70 nm) before the fiber. The effect of the cavity and the optical filters is demonstrated in Fig. 3b. The GG420 is used to avoid saturating the detector while maximizing the use of the detector in the region of interest. The band-pass filter was used to suppress the out of band light at longer wavelengths. If the spectrometer system has any issues with out of band light projection this can introduce stray light into the measurement spectra because the out of band light is orders of magnitude more intense than the measurement light in the region of interest. Light from the LED was collimated into the cavity by a 2 inch f/1 lens and focused onto the fiber after the cavity by a 1 inch f/4 lens (Thorlabs). The cavity and mirror mounts are designed so that the cavity can be enclosed using a 1 in. diameter stainless steel or Teflon tube.

After alignment the mirror reflectivity was determined using Rayleigh scattering as described in Washenfelder et al. (2008) by flowing helium in the cavity for a reference

AMTD
3, 2681–2721, 2010

spectrum followed by air or nitrogen:

$$R(\lambda) = 1 - d_0 \frac{\left(\frac{I_{N_2}(\lambda)}{I_{\mathrm{HE}}(\lambda)} \varepsilon_{\mathrm{Ray}}^{N2}(\lambda)\right) - \left(\varepsilon_{\mathrm{Ray}}^{\mathrm{He}}(\lambda)\right)}{1 - \left(\frac{I_{N_2}(\lambda)}{I_{\mathrm{HE}}(\lambda)}\right)}, \quad (2)$$

where d_0 is the cavity length and $\varepsilon_{\mathrm{Ray}}$ is the extinction due to Rayleigh scattering and I_{N2} and I_{He} are the intensities of the helium and nitrogen spectra, respectively.

2.1.3 The spectrometer and detector systems

The light exiting the cavity was focused onto an optical fiber. Two different sets of transfer optics and detector systems were used: (1) light was coupled via a 1 inch f/4 lens onto a 1mm diameter, f/4 glass optical fiber (Ocean Optics) which was coupled to an Ocean Optics QE65000 compact f/4 symmetrical-crossed Czerny-Turner spectrometer. This spectrometer has a 100 cm focal length and a 100 µm slit, and spectra were recorded using a 1.4 mm high Hamamatsu S7031–1006 (1024×58 pixels) CCD detector. The CCD chip was thermo electrically cooled to −10.±0.1 °C in order to reduce dark current of the detector. The spectrometer was heated to 31.±0.003 °C (above ambient) to remove temperature drifts in the wavelength pixel mapping of the spectrometer; (2) light was focused via the same lens onto a 1.5 mm diameter multi-mode single core optical fiber (Ceramoptic) coupled to 27 individual fibers that were distributed vertically in front of the slit of an Acton 2300i spectrometer, which was coupled with a PIXIS400 CCD Camera (Roper Scientific). The Acton 2300i had f/3.9 Czerny-Turner 300mm focal length spectrometer was used with a 1200 grooves/mm grating blazed at 450 nm. The PIXIS400 camera used a 8mm high 26.8 mm wide back illuminated CCD chip (e2v, 1340·400 pixels), that was thermoelectrically cooled to −75.±0.1 °C in order to reduce dark current. The spectrometer was heated to 35±0.1 °C. Both spectrometer/detector systems are fully integrated and controlled by the ATMOSpecLab data acquisition LabVIEW code. The code also reads up to eight temperatures, and contains four PID loops used to control and stabilize temperature.

AMTD
3, 2681–2721, 2010

2.1.4 Signal to noise comparison

The signal to noise of the two spectrometer/detector systems was evaluated using the root mean square (RMS) fit residual of the DOAS trace gas fit. The theoretical noise level was calculated using combination of the noise levels of the reference and the sample spectra taken in quadrature where the theoretical noise is: $N = \sqrt{N}/N$ (N being the maximum number of counts in the spectra). The integration time used to record the reference spectrum was two minutes for the QE65000, while the Acton/PIXIS reference was 3.5 min. Consecutive spectra were recorded with an integration time of 30 s and co-added to increase the photon counting statistics. Figure 4 compares the signal to noise ratio of the QE65000 and the Acton/PIXIS spectrometers. The Acton/PIXIS achieves a 2–3 times lower RMS noise for comparable integration times reflecting a 4–9 times higher light throughput. The higher light throughput is primarily due to the higher photon collection by the larger fiber and the better dispersal of light at the detector.

2.2 Aerosol generation and measurement

To characterize the performance of LED-CE-DOAS in the presence of aerosols, monodisperse aerosols of known size and refractive index were produced using the experimental setup shown in Fig. 2. Polystyrene latex spheres were used as the spherical size-selected aerosol test case. An aqueous solution of polystyrene latex spheres (PSLs, Thermo Scientific, 350 nm±7 nm) was prepared by suspending ten drops of standard in approximately 200 mL of de-ionized water. The solution was then volatilized using an atomizer. The airstream was subsequently dried using silica beads, and passed through a Scanning Mobility Particle Sizer (SMPS) which consists of a Differential Mobility Analyzer (DMA) (TSI model 3081) and a Condensation Particle Counter (CPC) (TSI 3022A, in high flow mode) used to size select and count particles. The SMPS was set to 5 lpm sheath flow and the sample flow through the DMA was 500 sccm. The size of the aerosols selected by the DMA is known to a 3% uncertainty (Biskos et al., 2006). Particles were counted by the CPC before and after passing

AMTD
3, 2681–2721, 2010

through the cavity, and numbers were found identical to within less than 1% indicating negligible particle losses inside the cavity. The mirrors were kept clean using a dry air purge at the ends of the cavity and the sample (aerosols and/or trace gases) was supplied in the middle of the enclosed cavity volume (Fig. 2).

2.3 Trace gas generation

Water was introduced in the flow volume after the aerosols had been selected by passing a dilution flow through a flask of de-ionized water (Fig. 2) and passed through a PFA Teflon filter in a PFA Teflon filter holder to remove any water droplets. Relative humidity (Honeywell, 4000-003, ±3.5%RH) and temperature (Omega RTD, ±0.01 °C) were measured at the center of the cavity, while pressure (MKS Baratron 629, ±0.12% of reading) was measured as the airstream exited the cavity. For closed cavity measurements, glyoxal, methyl glyoxal and NO_2 were generated, and supplied to the cavity as shown in Fig. 2. Air was bubbled through a solution of glyoxal and methyl glyoxal and then diluted before the cavity to provide both trace gases and water to the cavity. NO_2 was supplied from a standard bulb filled to a starting pressure of 830 Torr and a mixing ratio of 4×10^{-7} and then a small flow was leaked from the bulb, measured by a mass flow meter (Sierra Instruments) and diluted by the larger airstream. The NO_2 flow changed slowly over time as the pressure in the bulb reduced. The methyl glyoxal and glyoxal concentrations varied over time as a result of the difference in their respective Henry's Law coefficients (Betterton and Hoffmann, 1988; Ip et al., 2009).

Iodine monoxide measurements were made in closed-cavity mode. IO was generated via the reaction of ozone with iodine atoms as described by Martin et al. (2007). A 20 sccm flow of air was passed first through a flask that contained iodine crystals (Fisher Scientific) cooled in an ice bath and flowed into another flask equipped with an atomic Hg line emission lamp and a Xe line emission lamp (UVP). The Hg lamp was switched on briefly to produce ozone in the flask. The Xe lamp was on continuously, and produced iodine atoms by the photolysis of I_2, which then reacted with the ozone to make IO. The flow was diluted into a 1000 sccm total flow into the instrument.

AMTD
3, 2681–2721, 2010

After exiting the cavity an ozone monitor (ThermoFisher Scientific, 49i) measured the amount of ozone in the sample flow.

For open cavity measurements the tube enclosing the cavity was removed and a curtain flow was maintained on the mirrors, allowing both mirrors to face the open room air. NO_2 and water were present in the room air in sufficiently high concentrations that no further supply was needed. Glyoxal and methyl glyoxal were introduced to the light path by placing a row of Petri dishes containing solutions of glyoxal and methyl glyoxal directly under the light path.

3 Results and discussion

3.1 LED Light Source

The LEDengin LED used here is 5 times more powerful than the Luxeon and is more powerful than the calculated output of the Xe arc (Fig. 3a). The LED also overcomes the limitation created by the highly unstable Xe emission lines that fall in the middle of the CHOCHO evaluation range (see e.g., (Washenfelder et al., 2008). Because the LED emits less light at wavelengths where the mirror reflectivity drops (out of band light) than a Xe-arc lamp less filtering is needed to remove out of band light. Out of band light is orders of magnitude more intense than the sample light because of the drop in mirror reflectivity (more light allowed through the cavity). The reduced need for filtration allows for a wider useable wavelength range (420–490 nm) compared to arc lamp IBBCEAS setups (see Table 1).

Kern et al. (2006) pioneered the use of an LED light-source for long-path DOAS applications. They found the intensity of the 3W Luxeon Royal Blue LED to be approximately half that of a 450W Xe-arc lamp, but the LED produces two orders of magnitude more light for the power used (The Luxeon LED tested used by Kern et al. is a slightly different model and their LED had approximately twice the output of the Luxeon LED shown in Table 2 and Fig. 3). In addition, LEDs have lifetimes that exceed that of Xe-

AMTD
3, 2681–2721, 2010

arc lamps by a factor of 100, while reducing the cost by about a factor of 50 (Kern et al., 2006).

Another advantage of the LED that has been exploited in our CE-DOAS instrument is that the center wavelength of the LED can be chosen to match the wavelength of maximum mirror-reflectivity. This enables us to use the mirror in order to balance the light intensity across the detector. The effect of the mirror is illustrated in Fig. 3b, and enables us to measure a particularly broad spectral range that is 70 nm wide. This is about 2–3 times wider than previous CEAS instruments, see Table 1. This broader spectral range is a pre-requisite to measure the O_4 absorption band at 477 nm, together with the other gases. The O_4 absorption cross section is >10 times stronger at 477 nm than at 446 nm. That strong O_4 band, and the water bands at 443 nm provide us with independent means to measure the effective extinction length of photons from the cavity at two wavelengths, even under conditions where atmospheric turbulence or variable aerosol optical depth lead to light losses from the cavity that are variable in time. By measuring the decrease in the O_4 and H_2O SCDs compared to clean (aerosol free) air, CE-DOAS in principle allows for the differential measurement of aerosol optical depth.

3.2 DOAS retrieval and absorption cross section weighting

A data analysis routine has been developed using the WinDOAS spectral fitting program (Fayt and Van Roosendael, 2001). The algorithm uses as input the high-resolution molecular absorption cross-section spectra of glyoxal (296 K) (Volkamer et al., 2005c), methyl glyoxal (296 K) (Meller et al., 1991), O_4 (Hermans, 2010), H_2O (833 mbar, 296 K) (Rothman et al., 2006), NO_2 (294 K) (Vandaele et al., 2002) and IO (Hönninger, 1999). These spectra are convoluted with the slit function of the spectrometer and interpolated onto the wavelength dispersion of the spectrometer. Two fit ranges were used, one for the trace gases (435–465 nm) and one for O_4 (455–487 nm) each of these used a 4th order polynomial for the high pass filter. The cross-sections are then fitted to the measured optical density to retrieve the slant column density

AMTD
3, 2681–2721, 2010

(SCD, integrated concentration along a given path length). Other degrees of freedom of the non-linear least-square fitting routine are kept to a minimum in our retrieval, i.e., no spectral shift and intensity offset are allowed. The slant columns are converted to concentrations using the path length calibration.

DOAS uses a modified version of Lambert Beer's Law:

$$\ln\left(\frac{I_0}{I}\right) = \sigma(\lambda)cl(\lambda) \tag{3}$$

where I_0 and I are the reference and measurement intensities respectively and σ, c and l are the absorption cross-section, concentration and absorption path length, respectively. A modified form of Beer's Law is used that separates extinction processes as broadband and narrow-band (differential) processes.

$$\ln\left(\frac{I_0}{I}\right) = \left[\Sigma\sigma'(\lambda)c + \Sigma\sigma_b(\lambda)c + \varepsilon_{\text{Ray}} + \varepsilon_{\text{Mie}} + T(\lambda)\right]l \tag{4}$$

where σ' is the differential (narrow band) portion of the absorption cross-section, σ_b is the broadband component,, $\varepsilon_{Ray}$is the Rayleigh scattering, ε_{Mie} is the extinction from aerosols due to Mie scattering, and T is the instrument transfer function. A polynomial is then used to represent all broadband processes (σ_b, both Rayleigh and Mie scattering and T), while the trace gases of interest are identified by their characteristic differential absorption structure:

$$\ln\left(\frac{I_0}{I}\right) = \left[\Sigma\sigma'(\lambda)c + \text{polynomial}\right]l. \tag{5}$$

This application of Beer's law assumes that path length is constant within the wavelength interval used for the DOAS fit. However, in CEAS applications the effective path length varies strongly with wavelength. Equation (1) shows how it depends on the mirror reflectivity and all other extinction processes inside the cavity. The resulting wavelength dependence of path length will create residual structures if spectra are

AMTD
3, 2681–2721, 2010

linearly scaled in the respective DOAS fit windows. The effect is illustrated in Fig. 5. Systematic structures are visible in the fit residual that are clearly due to a glyoxal absorption feature at 440 nm. This is a direct effect of the cavity having a different path length at 440 nm than at 455 nm where glyoxal has the dominant absorption feature at our instrument resolution.

This effect is discussed in detail by Platt et al. (2009), and solutions to this problem exist either by means of interpolation of weighed absorption cross section spectra (Volkamer et al., 1998), or by an iterative approach (Frankenberg et al., 2005). We choose here to remove these residual structures by interpolation between two extreme cases. To create this cross-section, $\sigma(\bar{\lambda})$ we consider the combination of ?, the cross-section and L, the path length. We can account for the distortion in L by applying a correction factor $F(\lambda)$ to $\sigma(\lambda)$.:

$$\bar{\sigma}(\lambda) = \sigma(\lambda)F(\lambda) \tag{6}$$

Where $F(\lambda)$ is derived by calculating the path length according to Eq. (2) for a Rayleigh atmosphere, and then scaling this to the path length calculated at the dominant wavelength of the species of interest (477 nm for O_4, 455 nm for CHOCHO):

$$F(\lambda) = \frac{L\ (\lambda)}{L(\text{peak } \lambda \text{ of absorption})} \tag{7}$$

This method of accounting for spectral distortions varies from that presented in Platt et al. (2009). Their development of scaling factors for path length distortion requires a-priori knowledge of the total optical depth in the cavity, or D_{CE}. To our knowledge we present the first practical solution to the problem.

3.3 Determination of sample path, d_s

As depicted in Fig. 2, the aerosol and trace gas samples do not occupy the entire length of the cavity; the length of the volume (d_s) must be determined by a separate set of experiments. This is done by flowing a known amount of an absorber through the

AMTD
3, 2681–2721, 2010

sample portion of the cavity. In each run of the experiment before aerosols were introduced, humidified air was flowed through the cavity and the water vapor concentration was measured by the combination of relative humidity sensor, RTD and the pressure sensor. The ratio d_s/d_0 is then calculated as the ratio of the retrieved light path for the water (H_2O SCD divided by concentration calculated from the RH) and the theoretical path (Eq. 1) at the wavelength of the water band. The sample path is then calculated by multiplying this ratio by d_0. This can also be done using O_4 by flowing nitrogen in the purge volumes, and compressed air at known pressure in the cavity. Use of synthetic air requires characterization of the oxygen mixing ratio separately. In this experiment d_0=99.±0.1 cm and d_s=83±1 cm.

3.4 Order of DOAS O_4 fit Polynomial

In the DOAS retrieval fitting algorithm, using a polynomial is one means of numerical high pass filtering of spectra to represent all broadband extinction. The wavelength dependence of the mirror reflectivity is a primary factor that imposes a broadband shape to the collected spectra. When the cavity is filled with a non-absorbing gas, the light lost during n passes through the cavity is due to the reflectivity and the Raleigh scattering of the gas (Fig. 6a). If the cavity is sequentially filled with gases of different Rayleigh cross-sections, for example helium compared to nitrogen, or with air and aerosol compared to nitrogen only, the difference in the number of passes (n) is significant, and the mirror imposes its wavelength dependence on the intensity of the light according to a power law of R that has the difference of n as exponent. This variation in the number of times that R imposes its wavelength dependence needs to be captured by the numerical high pass filter. Sensitivity studies were carried out to determine the polynomial degree that is needed to capture this effect. It is found that a higher order polynomial (>3rd) is needed to account for the intensity change between the reference and the measurement spectra. If the dependence on the mirror reflectivity is not adequately accounted for, the mirror effect can cause an interference in the retrieved SCD of the O_4, which can lead to errors in the retrieved O_4 SCD by as much as 10% for

AMTD
3, 2681–2721, 2010

a 3rd degree polynomial. The sensitivity of the error in the retrieved O_4 SCD on the polynomial degree is illustrated in Fig. 6b, and c. Higher order polynomials significantly reduce this error. Figure 6b demonstrates that for the case of comparing a He and air spectrum, the observed O_4 matches to within better than 1% of the O_4 SCD inferred from knowledge of R and the Rayleigh cross section for a polynomial order of 4 and higher.

3.5 Methyl glyoxal measurement

In addition to glyoxal and NO_2, methyl glyoxal was detected with the LED-CE-DOAS instrument. The spectral proof is shown for an example retrieval in Fig. 5. The detection sensitivity of methyl glyoxal is approximately ten times less than that of glyoxal due to the smaller absorption cross-section. This lower sensitivity combined with the lower concentrations of methyl glyoxal make an atmospheric detection unlikely with our instrument. However, the sensitivity is high enough to be useful for the detection of methyl glyoxal in atmospheric simulation chambers where methyl glyoxal concentrations are higher. Detection limits for glyoxal, methyl glyoxal, IO, NO_2, water and O_4 were calculated conservatively by taking two times the RMS noise of the fit residual and dividing by the peak differential cross-section and the path length; in Table 3 typical values for the detection limit are given for the free troposphere (aerosol free) and an urban environment (aerosol extinction=5×10^{-6} cm^{-1}).

3.6 IO and I_2 measurement

IO was measured by the instrument in the presence of I_2 and ozone. Both the ozone absorption in the Huggins band, and the molecular iodine absorption provide broadband extinctions in the cavity. Because the measured ozone concentration (<20 ppbv, an extinction of 2×10^{-10} cm^{-1} at 477 nm) was not high enough to change the path length in the cavity; absorption by iodine was then the only broadband extinction process within the DOAS analysis windows. This allowed the I_2 concentration to be re-

AMTD
3, 2681–2721, 2010

trieved in a similar manner to the aerosol extinction (with the assumption that no aerosol was present) by the measurement of O_4 (Eq. 9). The I_2 concentration was then used in combination with the wavelength dependence of the I_2 spectrum, and the mirror reflectivity curve to calculate the absorption path length for IO. Sample spectra are shown in Fig. 7a. A 1.5 pptv minimum detection limit for IO for a 2 min integration time using the QE65000 spectrometer was calculated (Fig. 7b). The somewhat lower detection sensitivity towards IO in this experiment compared to that listed in Table 3 is due to the greatly reduced path length and higher RMS above 450 nm caused by the I_2 absorption for concentration that is orders of magnitude higher than that found in the marine background.

3.7 Aerosol extinction measurements

Aerosols contribute to the largest possible extinction process that reduces the path length in the cavity (see Fig. 1). Aerosol extinction can be inferred from the change in the measured path in the presence of aerosols, compared to the path in the empty cavity (determined by separate measurements of R, Sect. 2.1.2, and knowledge of the Rayleigh scattering cross section of air, and air pressure). The aerosol extinction was calculated using a modified version of the path length equation (1), with the substitution of d_s (the sample length) for d_0 (the cavity length) for aerosols and trace gases:

$$\varepsilon_{\text{aer}}(\lambda) = \frac{\left(\frac{d_0}{\overline{L_{\text{aer}}(\lambda)}}\right) - 1 + R(\lambda) - \varepsilon_{\text{Ray}}(\lambda) d_0}{d_s}. \quad (8)$$

This can be simplified if the sample path for the aerosols and the reference absorber are the same, where L_{aer} is the path in the presence of aerosols and L_0 is the path in

AMTD
3, 2681–2721, 2010

a clean cavity:

$$\varepsilon_{\mathrm{aer}}(\lambda) = \left(\frac{d_0}{d_s}\right)\left(\frac{1}{\overline{L_{\mathrm{aer}}}(\lambda)} - \frac{1}{\overline{L_0}(\lambda)}\right) = \frac{d_0}{d_s}(O_{2vmr}{}^2)\left(\frac{1}{\frac{O_4\mathrm{SCD}_{\mathrm{aer}}}{N_{d,\mathrm{aer}}{}^2}} - \frac{1}{\frac{O_{4\mathrm{SCD}}}{N_{d^2}}}\right) \quad (9)$$

where d_0 and d_S are defined in Sect. 3.3, N_d is the density of air (N_d = 2.09×10^{19} molecules cm^{-3} (at a pressure of 830 mbar and a temperature of 298 K), $O_{2,mr}$ is the oxygen mixing ratio of air, the O_4 SCD term is the column density of the oxygen dimer in pure are and is equivalent to L_0 as defined in Eq (1), $\varepsilon_{\mathrm{Ray}}$ is the extinction due to Rayleigh scattering and O_4 $\mathrm{SCD}_{\mathrm{aer}}$ is measured. Two different approaches were used to retrieve the aerosol extinction. The first approach used the change in the retrieved SCD of O_4 at 477 nm combined with the independent measurement of pressure and temperature and the knowledge of the oxygen mixing as given in Eq. (9). The second used a modified version of Eq. (9), using the SCD of water measured at 443 nm in a similar fashion to O_4, and relative humidity, pressure and temperature were measured separately to calculate the number density of water molecules in cm^3 of air. The detection limit for aerosol extinction is 1.6×10^{-8} cm^{-1} at 477 nm and 1×10^{-7} cm^{-1} at 443 nm.

3.8 Comparison to Mie theory

The aerosol extinctions as retrieved from the reduction of the path length in the cavity were compared to Mie theory. The wavelength dependence of the refractive index of the mono-disperse PSLs was calculated based on the Cauchy expression terms given in the PSL datasheet (ThermoFisher Scientific Technical Note TN007.03). The aerosol scattering cross-section was then calculated using Mie theory. The scattering cross-section for a 350±15 nm PSL ($\sigma_{443\mathrm{nm}}$=3.54×10^{-9} cm^2, $\sigma_{477\mathrm{nm}}$= 2.84×10^{-9} cm^2) was multiplied by the measured aerosol concentration to calculate the aerosol extinction in the cavity. There was no need to apply a correction for doubly charged parti-

AMTD
3, 2681–2721, 2010

cles (Wiedensohler, 1988) because only one size of particle was supplied to the DMA which was primarily used to remove bead aggregates and surfactant particles that were also produced by the atomizer (Miles et al., 2010). A conservative uncertainty of ±4% (±15 nm) in the size-selected particle diameter is assumed based on the reported sensitivity of the SMPS (Biskos et al., 2006) and the size distribution in the PSL standard. As can be seen in Fig. 8 for aerosol with NO_2, and in Fig. 9 for aerosol with glyoxal and methyl glyoxal, the aerosol extinction retrieved from the change in the O_4 SCD by Eq. (9) agreed within error bars with the Mie theory calculations at 477 nm (Fig. 8b, 9b) and 443 nm (Fig. 8c). The measurement of the aerosol extinction at two wavelengths allows us to interpolate the wavelength dependence of the aerosol extinction for the NO_2 experiment. For the glyoxal and methyl glyoxal experiment the known wavelength dependence of the aerosol extinction was used with the mirror reflectivity to retrieve the path length for the glyoxal and methyl glyoxal. The retrieved λ^{-n} dependence ($\lambda^{-3.8\pm2.1}$) of the extinction matches well with the dependence calculated from Mie theory (λ^{-3}). The variability is still large due to the measurement of the aerosol extinction at the water wavelength that is currently limited by the accuracy in the RH measurement and the accuracy with which the water absorption cross sections are known. In practice, inferences of the wavelength dependence of aerosol extinction are more precise by measuring a gas which absorbs over a broad wavelength range, e.g., NO_2, at 477 nm (the O_4 wavelength), and use the known wavelength dependence of that gas to derive the wavelength dependence of aerosol extinction.

3.9 Open Cavity Detection of NO_2, glyoxal and methyl glyoxal

The inherent O_4 path length calibration of our LED-CE-DOAS instrument enables its use in open cavity mode. The concentrations of NO_2, glyoxal and methyl glyoxal were measured simultaneously in laboratory room air with the cavity operating in open cavity mode. Figure 10 shows the retrievals of these trace gases from spectra that were recorded in open cavity mode. Path length for glyoxal and methyl glyoxal were retrieved by using the O_4 path to measure the NO_2 concentration and then using the NO_2 con-

AMTD
3, 2681–2721, 2010

centration and SCD in the glyoxal fit window to retrieve the path length for the desired trace gases as described above. Using the inherent path length calibration, the room air between the mirrors was characterized to be composed of: NO_2, methyl glyoxal and glyoxal of 2.47±0.07 ppbv, 1.2±0.2 pbbv, and 274±14 pptv, respectively and an aerosol extinction measured from O_4 of $4\pm3\times10^{-8}$ cm^{-1}. This is to our knowledge the first well calibrated CEAS measurement in open air.

4 Conclusions

We have demonstrated the first well calibrated CEAS measurement in open cavity mode. Previous CEAS measurements either removed aerosols by means of filtration in sampling lines, or required separate calibration measurements. Further, a first CEAS measurement is demonstrated for methyl glyoxal, and aerosol extinction at 443 nm and 477 nm; the first CE-DOAS detection of glyoxal and iodine oxide are accomplished.

- The innovative use of the blue high optical output LED light source has advantages over traditional Xe-arc lamps that help reduce instrument size, and add to instrument sensitivity, reliability and portability. (1) The 5W electrical power LED is found to be brighter than a 450W Xe-arc lamp in the wavelength range of interest, (2) the LED is smaller, (3) longer lived, (4) more cost effective, and (5) can be powered with standard laboratory power supplies. Finally, (6) the LED emission spectrum is unstructured, and constant in time, which helps to make the blue spectral range more accessible for DOAS applications.
- Use of the LED is also a prerequisite for the inherent path length calibration. The LED is optimally paired with mirror reflectivity, which (7) enables a better balance of light intensity across the detector, (8) eliminates the need for more narrow optical filters that limit the band-width and (9) enables us to significantly broaden the useable spectral range (70 nm) compared to previous CEAS arrangements (see Table 1).

AMTD
3, 2681–2721, 2010

– This inherent path length calibration is the direct result of the wide spectral range, and is based on measurements of a strong O_4 absorption band at 477 nm at atmospheric conditions as part of each spectrum with good signal to noise. The path length calculation only requires knowledge of gas-density as input. Similarly, measurements of the H_2O SCD, in combination with relative humidity and temperature facilitate the inherent path length calibration at 443 nm.

– The first CEAS use to retrieve aerosol extinction at two wavelengths with a single optical cavity is accomplished. The approach was demonstrated by comparing the retrieved aerosol extinction to Mie theory. Knowledge of the wavelength dependent aerosol extinction is a prerequisite to accurately infer the wavelength dependence of the effective path length in the presence and absence of aerosols.

– Our LED-CE-DOAS instrument is most sensitive if the cavity is kept aerosol free. However, also in the presence of aerosols the sensitivity is found suitable for atmospheric measurements of glyoxal, iodine oxide, nitrogen dioxide and aerosol extinction in polluted and pristine air. The sensitivity is useful to detect methyl glyoxal directly under simulated atmospheric conditions in chambers.

– The first measurements of NO_2, water, glyoxal, methyl glyoxal and aerosol extinction at two wavelengths in open cavity mode are demonstrated (mirrors facing the open atmosphere). The open cavity mode eliminates the need for sampling lines, and is particularly useful for measurements of reactive gases and radicals, which can get lost in sampling lines.

– Our approach of inherent path length calibration enables the use of optical cavities in analogy to White-type and Herriott-type multi-reflection cells for which the number of reflections is geometrically defined, and constant. The benefits of knowing the number of reflections in the optical cavity as part of each spectrum enables the use of optical cavities as direct alternatives to traditional multi-reflection cells.

AMTD
3, 2681–2721, 2010

The benefit are 100–1000 times longer photon path length, and accordingly higher sensitivity.

Acknowledgements. This work was supported by the National Science Foundation CAREER award ATM-847793, CU start-up funds and NASA Earth and Space Science Fellowship 09-EARTH09F-88. The authors like to thank Jose Luis Jimenez, Steve Brown, Rebecca Washenfelder, and Christa Hasenkopf for use of calibration equipment, and helpful discussions, Barbara Dix and Eleanor Waxman provided guidance on the WinDOAS software package, and comments on the manuscript.

References

Ball, S. M., Langridge, J. M., and Jones, R. L.: Broadband cavity enhanced absorption spectroscopy using light emitting diodes, Chem. Phys. Lett., 398, 68–74, 2004.

Betterton, E. A. and Hoffmann, M. R.: Henry's law constants of some environmentally important aldehydes, Envir. Sci. Technol., 22, 1415–1418, 1988.

Biskos, G., Paulsen, D., Russell, L. M., Buseck, P. R., and Martin, S. T.: Prompt deliquescence and efflorescence of aerosol nanoparticles, Atmos. Chem. Phys., 6, 4633–4642, doi:10.5194/acp-6-4633-2006, 2006.

Bloss, C., Wagner, V., Bonzanini, A., Jenkin, M. E., Wirtz, K., Martin-Reviejo, M., and Pilling, M. J.: Evaluation of detailed aromatic mechanisms (MCMv3 and MCMv3.1) against environmental chamber data, Atmos. Chem. Phys., 5, 623–639, doi:10.5194/acp-5-623-2005, 2005.

Brown, S. S.: Absorption spectroscopy in high-finesse cavities for atmospheric studies, Chem. Rev., 103, 5219–5238, 2003.

Dibble, T. S.: Intramolecular Hydrogen Bonding and Double H-Atom Transfer in Peroxy and Alkoxy Radicals from Isoprene, J. Phys. Chem. A, 108, 2199–2207, 2004a.

Dibble, T. S.: Prompt Chemistry of Alkenoxy Radical Products of the Double H-Atom Transfer of Alkoxy Radicals from Isoprene, J. Phys. Chem. A, 108, 2208–2215, 2004b.

Dixneuf, S., Ruth, A. A., Vaughan, S., Varma, R. M., and Orphal, J.: The time dependence of molecular iodine emission from Laminaria digitata, Atmos. Chem. Phys., 9, 823–829, doi:10.5194/acp-9-823-2009, 2009.

Fayt, C. and Van Roosendael, M.: WinDOAS User Manual, 2001.

AMTD

3, 2681–2721, 2010

Fiedler, S. E., Hese, A., and Ruth, A. A.: Incoherent broad-band cavity-enhanced absorption spectroscopy, Chem. Phys. Lett., 371, 284–294, 2003.
Frankenberg, C., Platt, U., and Wagner, T.: Iterative maximum a posteriori (IMAP)-DOAS for retrieval of strongly absorbing trace gases: Model studies for CH4 and CO_2 retrieval from near infrared spectra of SCIAMACHY onboard ENVISAT, Atmos. Chem. Phys., 5, 9–22, doi:10.5194/acp-5-9-2005, 2005.
Fu, T. M., Jacob, D. J., Wittrock, F., Burrows, J. P., Vrekoussis, M., and Henze, D. K.: Global budgets of atmospheric glyoxal and methylglyoxal, and implications for formation of secondary organic aerosols, J. Geophys. Res., 113, doi:10.1029/2007JD009505, D15303, 2008.
Galloway, M. M., Chhabra, P. S., Chan, A. W. H., Surratt, J. D., Flagan, R. C., Seinfeld, J. H., and Keutsch, F. N.: Glyoxal uptake on ammonium sulphate seed aerosol: reaction products and reversibility of uptake under dark and irradiated conditions, Atmos. Chem. Phys., 9, 3331–3345, doi:10.5194/acp-9-3331-2009, 2009.
Gherman, T., Venables, D. S., Vaughan, S., Orphal, J., and Ruth, A. A.: Incoherent broadband cavity-enhanced absorption spectroscopy in the near-ultraviolet: Application to HONO and NO_2, Envir. Sci. Technol., 42, 890–895, 2008.
Hastings, W. P., Koehler, C. A., Bailey, E. L., and De Haan, D. O.: Secondary organic aerosol formation by glyoxal hydration and oligomer formation: Humidity effects and equilibrium shifts during analysis, Envir. Sci. Technol., 39, 8728–8735, 2005.
Hermans, C.,Measurement of absorption cross sections and spectroscopic molecular parameters: O_2 and its collisonal induced absorption: http://www.aeronomie.be/spectrolab/o2.htm4-9-20104-26-3010.
Herriott, D. R. and Schulte, H. J.: Folded Optical Delay Lines, Appl.Opt., 4, 883–889, 1965.
Hönninger, G.: Referenzspektren reaktiver Halogenverbindungen für DOAS-Messungen, 1999.
Huisman, A. J., Hottle, J. R., Coens, K. L., DiGangi, J. P., Galloway, M. M., Kammrath, A., and Keutsch, F. N.: Laser-Induced Phosphorescence for the in Situ Detection of Glyoxal at Part per Trillion Mixing Ratios, Anal. Chem., 80, 5884–5891, 2008.
Ip, H. S. S., Huang, X. H. H., and Yu, J. Z.: Effective Henry's law constants of glyoxal, glyoxylic acid, and glycolic acid, Geophys. Res. Lett., 36, L01802, doi:10.1029/2008GL036212, 2009.
Jang, M., Czoschke, N. M., Lee, S., and Kamens, R. M.: Heterogeneous Atmospheric Aerosol Production by Acid-Catalyzed Particle-Phase Reactions, Science, 298, 814–817, 2002.
Kern, C., Trick, S., Rippel, B., and Platt, U.: Applicability of light-emitting diodes as light sources

AMTD
3, 2681–2721, 2010

for active differential optical absorption spectroscopy measurements, Appl. Opt., 45, 2077–2088, 2006.
Kurosu, T., Chance, K., and Volkamer, R.: Global measurements of OClO, BrO, HCHO, and CHO-CHO from the Ozone Monitoring Instruments on EOS Aura, EOS Trans. EGU, 86, Fall Meet. Suppl. Abstract A54B-01, 2005.
Langridge, J. M., Ball, S. M., and Jones, R. L.: A compact broadband cavity enhanced absorption spectrometer for detection of atmospheric NO_2 using light emitting diodes, Analyst, 131, 916–922, 2006.
Langridge, J. M., Ball, S. M., Shillings, A. J. L., and Jones, R. L.: A broadband absorption spectrometer using light emitting diodes for ultrasensitive, in situ trace gas detection, Rev. Sci. Instrum., 79, 2008a.
Langridge, J. M., Laurila, T., Watt, R. S., Jones, R. L., Kaminski, C. F., and Hult, J.: Cavity enhanced absorption spectroscopy of multiple trace gas species using a supercontinuum radiation source, Opt. Express, 16, 10178–10188, 2008b.
Liggio, J., Li, S. M., and McLaren, R.: Reactive uptake of glyoxal by particulate matter, J. Geophys. Res., 110, doi:10.1029/2004JD005113, D10304, 2005.
Martin, J. C. G., Spietz, P., and Burrows, J. P.: Kinetic and mechanistic studies of the I-2/O-3 photochemistry, J. Phys. Chem. A, 111, 306–320, 2007.
Meinen, J., Thieser, J., Platt, U., and Leisner, T.: Using a high finesse optical resonator to provide a long light path for differential optical absorption spectroscopy: CE-DOAS, Atmos. Meas. Tech., 8, 10665–10695, 2008, http://www.atmos-meas-tech.net/8/10665/2008/.
Meller, R., Raber, W., Crowley, J. N., Jenkin, M. E., and Moortgat, G. K.: The UV-visible absorption spectrum of methylglyoxal, J. Photochem. Photobio., A, 62, 163–171, 1991.
Miles, R. E. H., Rudic, S., Orr-Ewing, A. J., and Reid, J. P.: Measurements of the wavelength dependent extinction of aerosols by cavity ring down spectroscopy, Phys. Chem. Chem. Phys., 12, 3914–3920, 2010.
Myriokefalitakis, S., Vrekoussis, M., Tsigaridis, K., Wittrock, F., Richter, A., Brühl, C., Volkamer, R., Burrows, J. P., and Kanakidou, M.: The influence of natural and anthropogenic secondary sources on the glyoxal global distribution, Atmos. Chem. Phys., 8, 4965–4981, doi:10.5194/acp-8-4965-2008, 2008.
Okeefe, A. and Deacon, D. A. G.: Cavity Ring-Down Optical Spectrometer for Absorption-Measurements Using Pulsed Laser Sources, Rev. Sci. Instrum., 59, 2544–2551, 1988.

AMTD
3, 2681–2721, 2010

Orphal, J. and Ruth, A. A.: High-resolution Fourier-transform cavity-enhanced absorption spectroscopy in the near-infrared using an incoherent broad-band light source, Opt. Express, 16, 19232–19243, 2008.

Platt, U., Meinen, J., Pöhler, D., and Leisner, T.: Broadband Cavity Enhanced Differential Optical Absorption Spectroscopy (CE-DOAS) - applicability and corrections, Atmos. Meas. Tech., 2, 713-723, doi:10.5194/amt-2-713-2009, 2009.

Platt, U. and Stutz, J.: Differential optical absorption spectroscopy: principles and applications, 1, Springer Verlag, Berlin, Germany, 2008.

Pope, C. A. and Dockery, D. W.: Health effects of fine particulate air pollution: Lines that connect, J. Air Waste Manage. Assoc., 56, 709–742, 2006.

Rothman, L. S., Gordon, I. E., Barbe, A., Benner, D. C., Bernath, P. F., Birk, M., Boudon, V., Brown, L. R., Campargue, A., Champion, J. P., Chance, K., Coudert, L. H., Dana, V., Devi, V. M., Fally, S., Flaud, J. M., Gamache, R. R., Goldman, A., Jacquemart, D., Kleiner, I., Lacome, N., Lafferty, W. J., Mandin, J. Y., Massie, S. T., Mikhailenko, S. N., Miller, C. E., Moazzen-Ahmadi, N., Naumenko, O. V., Nikitin, A. V., Orphal, J., Perevalov, V. I., Perrin, A., Predoi-Cross, A., Rinsland, C. P., Rotger, M., Simeckovβ, M., Smith, M. A. H., Sung, K., Tashkun, S. A., Tennyson, J., Toth, R. A., Vandaele, A. C., and Vander Auwera, J.: The HITRAN 2008 molecular spectroscopic database, J. Quant. Spectrosc. Radiat. Transfer, 110, 533–572, 2006.

Schuster, G., Labazan, I., and Crowley, J. N.: A cavity ring down/cavity enhanced absorption device for measurement of ambient NO_3 and N_2O_5, Atmos. Meas. Tech., 2, 1–13, doi:10.5194/amt-2-1-2009, 2009.

Sihler, H., Kern, C., Pohler, D., and Platt, U.: Applying light-emitting diodes with narrowband emission features in differential spectroscopy, Opt.Lett., 34, 3716–3718, 2009.

Sinreich, R., Volkamer, R., Filsinger, F., Frieß, U., Kern, C., Platt, U., Sebastián, O., and Wagner, T.: MAX-DOAS detection of glyoxal during ICARTT 2004, Atmos. Chem. Phys., 7, 1293–1303, doi:10.5194/acp-7-1293-2007, 2007.

Stavrakou, T., Müller, J.-F., De Smedt, I., Van Roozendael, M., Kanakidou, M., Vrekoussis, M., Wittrock, F., Richter, A., and Burrows, J. P.: The continental source of glyoxal estimated by the synergistic use of spaceborne measurements and inverse modelling, Atmos. Chem. Phys., 9, 8431–8446, doi:10.5194/acp-9-8431-2009, 2009.

Taraborrelli, D., Lawrence, M. G., Butler, T. M., Sander, R., and Lelieveld, J.: Mainz Isoprene Mechanism 2 (MIM2): an isoprene oxidation mechanism for regional and global atmospheric

AMTD
3, 2681–2721, 2010

modelling, Atmos. Chem. Phys., 9, 2751–2777, doi:10.5194/acp-9-2751-2009, 2009.
Triki, M., Cermak, P., Mejean, G., and Romanini, D.: Cavity-enhanced absorption spectroscopy with a red LED source for NOx trace analysis, Appl. Phys. B, 91, 195–201, 2008.
Vandaele, A. C., Hermans, C., Fally, S., Carleer, M., Colin, R., Merienne, M. F., Jenouvrier, A., and Coquart, B.: High-resolution Fourier transform measurement of the NO_2 visible and near-infrared absorption cross sections: Temperature and pressure effects, J. Geophys. Res., 107, 4348, doi:10.1029/2001JD000971, 2002.
Varma, R. M., Venables, D. S., Ruth, A. A., Heitmann, U., Schlosser, E., and Dixneuf, S.: Long optical cavities for open-path monitoring of atmospheric trace gases and aerosol extinction, Appl. Opt., 48, B159–B171, 2009.
Vaughan, S., Gherman, T., Ruth, A. A., and Orphal, J.: Incoherent broad-band cavity-enhanced absorption spectroscopy of the marine boundary layer species I-2, IO and OIO, Phys. Chem. Chem. Phys., 10, 4471–4477, 2008.
Venables, D. S., Gherman, T., Orphal, J., Wenger, J. C., and Ruth, A. A.: High sensitivity in situ monitoring of NO_3 in an atmospheric simulation chamber using incoherent broadband cavity-enhanced absorption spectroscopy, Envir. Sci. Technol., 40, 6758–6763, 2006.
Villalobos-Pietrini, R., Hernandez-Mena, L., Amador-Munoz, O., Munive-Colin, Z., Bravo-Cabrera, J. L., Gómez-Arroyo, S., Frias-Villegas, A., Waliszewski, S., Ramirez-Pulido, J., and Ortiz-Muniz, R.: Biodirected mutagenic chemical assay of PM10 extractable organic matter in Southwest Mexico City, Mutat.Res./Gen.Toxicol.Environ.Mutag., 634, 192–204, 2007.
Volkamer, R., Barnes, I., Platt, U., Molina, L. T., and Molina, M. J.: Remote Sensing of Glyoxal by Differential Optical Absorption Spectroscopy (DOAS): Advancements in Simulation Chamber and Field Experiments, 2005a.
Volkamer, R., Coburn, S., Dix, B., and Sinreich, R.: The Eastern Pacific Ocean is a source for short lived trace gases: Glyoxal and Iodine Oxide, April, 2010.
Volkamer, R., Etzkorn, T., Geyer, A., and Platt, U.: Correction of the oxygen interference with UV spectroscopic (DOAS) measurements of monocyclic aromatic hydrocarbons in the atmosphere, Atmos. Environ., 32, 3731–3747, 1998.
Volkamer, R., Ziemann, P. J., and Molina, M. J.: Secondary Organic Aerosol Formation from Acetylene ($C2H_2$): seed effect on SOA yields due to organic photochemistry in the aerosol aqueous phase, Atmos. Chem. Phys., 9, 1907–1928, doi:10.5194/acp-9-1907-2009, 2009.
Volkamer, R., Molina, L. T., Molina, M. J., Shirley, T., and Brune, W. H.: DOAS measurement of glyoxal as an indicator for fast VOC chemistry in urban air, Geophys. Res. Lett., 32, L08806,

AMTD
3, 2681–2721, 2010

doi:10.1029/2005GL022616, 2005b.
Volkamer, R., San Martini, F., Molina, L. T., Salcedo, D., Jimenez, J. L., and Molina, M. J.: A missing sink for gas-phase glyoxal in Mexico City: Formation of secondary organic aerosol, Geophys. Res. Lett., 34, L19807, doi:10.1029/2007GL030752, 2007.
Volkamer, R., Spietz, P., Burrows, J., and Platt, U.: High-resolution absorption cross-section of glyoxal in the UV-vis and IR spectral ranges, J. Photochem. Photobio., A, 172, 35–46, 2005c.
Vrekoussis, M., Wittrock, F., Richter, A., and Burrows, J. P.: Temporal and spatial variability of glyoxal as observed from space, Atmos. Chem. Phys., 9, 4485–4504, doi:10.5194/acp-9-4485-2009, 2009.
Washenfelder, R. A., Langford, A. O., Fuchs, H., and Brown, S. S.: Measurement of glyoxal using an incoherent broadband cavity enhanced absorption spectrometer, Atmos. Chem. Phys., 8, 7779–7793, doi:10.5194/acp-8-7779-2008, 2008.
White, J. U.: Long Optical Paths of Large Aperture, J. Opt. Soc. Am., 32, 285–288, 1942.
Wiedensohler, A.: An approximation of the bipolar charge distribution for particles in the submicron size range, J. Aerosol Sci., 19, 387–389, 1988.
Wittrock, F., Richter, A., Oetjen, H., Burrows, J. P., Kanakidou, M., Myriokefalitakis, S., Volkamer, R., Beirle, S., Platt, U., and Wagner, T.: Simultaneous global observations of glyoxal and formaldehyde from space, Geophys. Res. Lett., 33, L16804, doi:10.1029/2006GL026310, 2006.
Wu, T., Zhao, W., Chen, W., Zhang, W., and Gao, X.: Incoherent broadband cavity enhanced absorption spectroscopy for in situ measurements of NO_2 with a blue light emitting diode, Appl. Phys. B, 94, 85–94, 2009.

AMTD
3, 2681–2721, 2010

Table 1. Summary of previous CEAS instruments in the blue spectral range.

Light Source	Mirror Reflectivity	Useable Spectral Range (nm)	Detected Species	Reference
Xe Arc	1. 0.999 2. 0.9998	1. 415–450 2. 427–450	IO IO	(Vaughan et al., 2008)
Xe Arc	0.99996	440–465	CHOCHO, NO_2, H_2O	(Washenfelder et al., 2008)
LED	0.99976	440–460	NO_2, O_4	(Langridge et al., 2006)
LED	0.997	450–490	NO_2	(Wu et al., 2009)
LED	0.99996	420–490	CHOCHO CH_3COCHO, IO, NO_2, O_4, H_2O	This work

AMTD
3, 2681–2721, 2010

Table 2. Properties of tested LEDs in the blue spectral range.

Company	Color	Model #	Peak λ (nm)	Etalon (Y/N)	Electrical Power (W)	Optical Power (W)	Chip Size (µm×µm)
Phillips-Luxeon	Blue	LXK2-PB14-P00	470	Y	3	0.216	992·992
Phillips-Luxeon	Royal Blue	LXK2-PR14-P00	455	Y	3	0.273	992·992
Seoul Semiconductor	Blue	B11190	465	N	1	0.180	755·755
LedEngin	Blue	LZ1-00B205	465	N	5	1.3	1000·1000

AMTD
3, 2681–2721, 2010

Table 3. Detection Limits for species in an aerosol free and an urban environment ($\varepsilon_{aer}=5\times10^{-6}$ cm^{-1} at 450 nm).

Species Detected in 1 min	Aerosol Free (L=15 km)	Urban Environment (L=1.8 km)
CHOCHO	22 pptv	190 pptv
CH_3COCHO	200 pptv	1.5 ppbv
NO_2	37 pptv	290 pptv
IO	0.5 pptv	4.3 pptv
Water	340 ppm	0.3%
O_4	0.1% mixing ratio O_2	0.8%

AMTD
3, 2681–2721, 2010

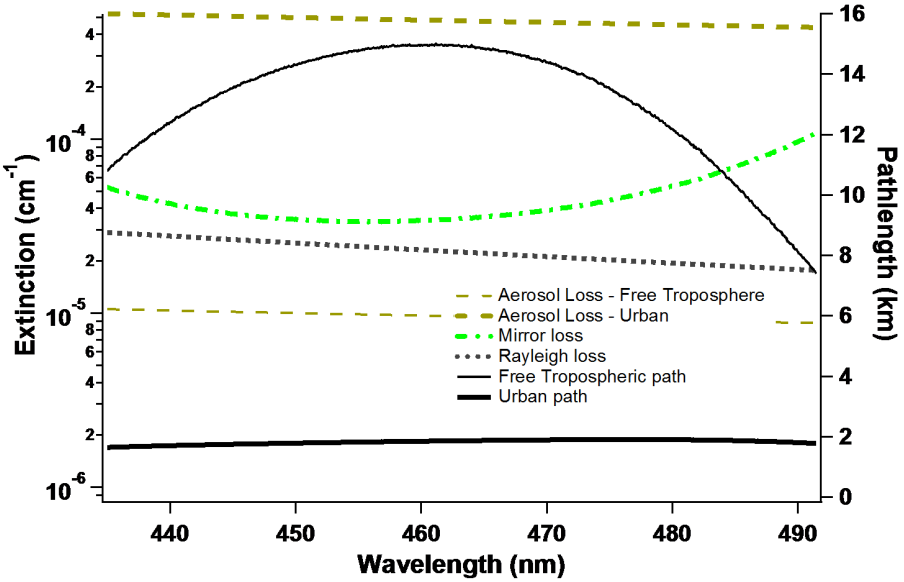

Fig. 1. Effect of aerosols to reduce the effective path length. The wavelength dependent extinction losses (dotted lines) are: mirror loss (1-R) of our cavity (green dashed – dotted line), Rayleigh scattering loss of air at 1 atm (gray dotted line), and aerosol losses for two scenarios: free tropospheric conditions (AOD=1×10^{-7} cm^{-1} at 450 nm, thin dashed line); and polluted urban conditions (2.5×10^{-6} cm^{-1} at 450 nm, thick dashed line). The wavelength dependence of aerosol extinction was approximated as λ^{-3}. The corresponding effective path length for both scenarios is shown by the respective solid lines.

AMTD
3, 2681–2721, 2010

Inherent calibration of a LED-CE-DOAS instrument

R. Thalman and R. Volkamer

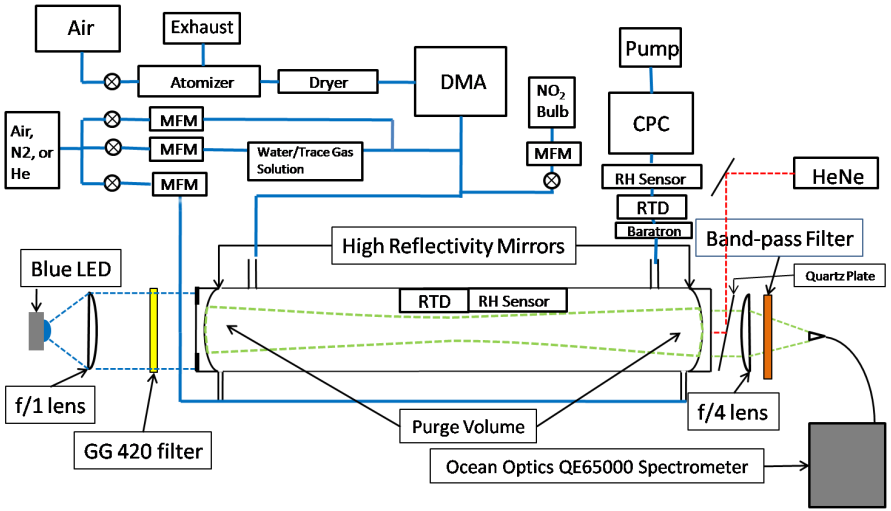

Fig. 2. Schematic of the cavity set up and flow handling system for aerosol delivery.

AMTD
3, 2681–2721, 2010

Inherent calibration of a LED-CE-DOAS instrument

R. Thalman and R. Volkamer

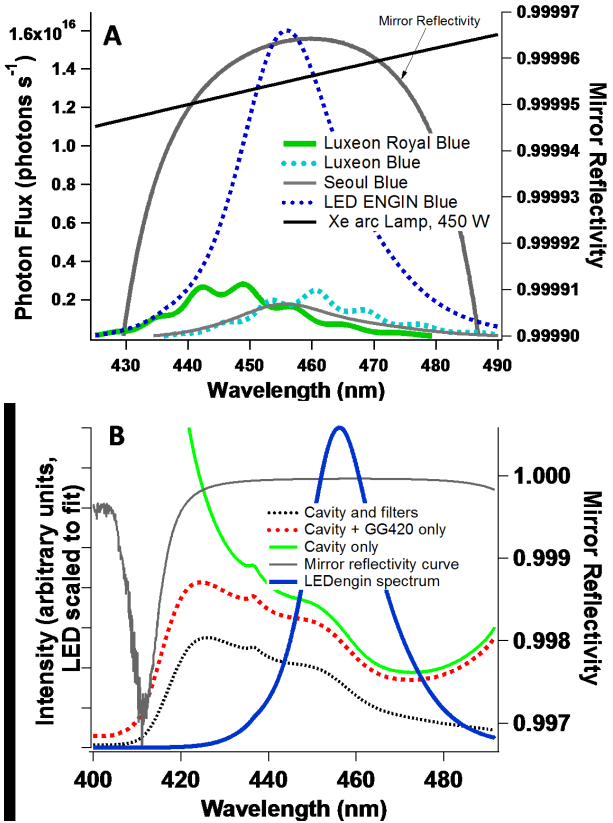

Fig. 3. **(A)** Emission spectra of several LEDs and a Xe arc lamp compared to the mirror reflectivity curve. **(B)** Sample measurement to illustrate the effect of the cavity mirrors and optical filter elements (cavity mirrors, GG420 cut-off filter, band-pass filter) on spectral intensity.

AMTD
3, 2681–2721, 2010

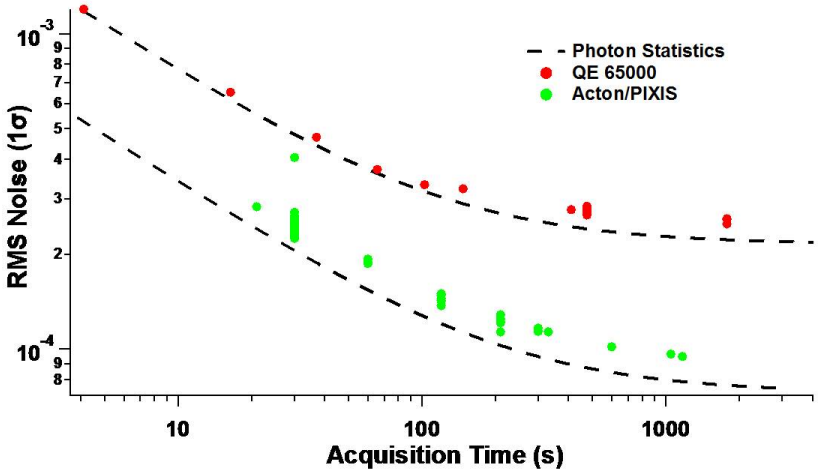

Fig. 4. RMS Photon noise as a function of acquisition time as measured by the two spectrometer/detector systems used in this study. The calculated photon shot-noise limit is shown by the dashed lines.

AMTD
3, 2681–2721, 2010

Inherent calibration of a LED-CE-DOAS instrument

R. Thalman and R. Volkamer

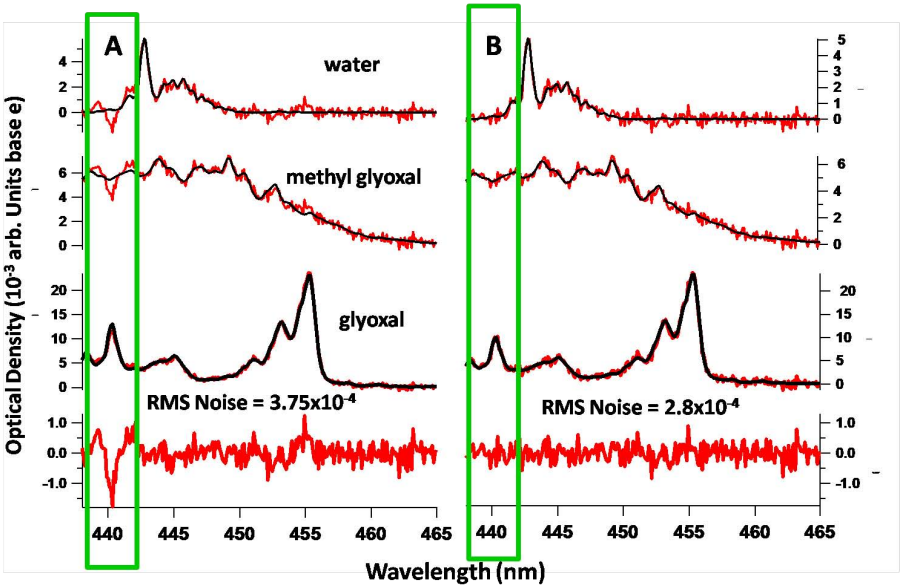

Fig. 5. Effects of wavelength dependent path length on the fit residual. **(A)** An unscaled glyoxal cross-section is fitted to the spectra. **(B)** Scaled glyoxal cross-section fit. Cross-section scaling is able to reduce the RMS by eliminating systematic residual structures. The experimental conditions are: [glyoxal]=1.45 ppbv, [methylglyoxal]=2.05 ppbv, [H_2O]=0.59%.

AMTD
3, 2681–2721, 2010

Inherent calibration of a LED-CE-DOAS instrument

R. Thalman and R. Volkamer

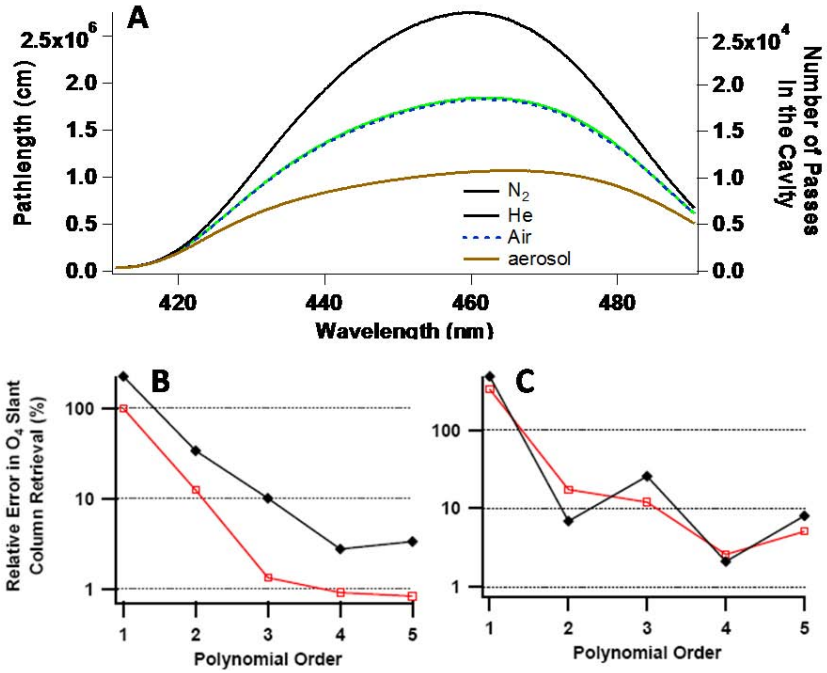

Fig. 6. Effect of mirror reflectivity and high pass filter on the O_4 retrieval. Panel **(A)**: Average path length and number of traverses in the cavity in helium (black), nitrogen (green), air (blue) and air with aerosol (brown, $\alpha_{aer}=3\times10^{-7}$ cm^{-1}); Panel **(B)**: The relative error in the retrieved O_4 slant column retrieved compared to the calculated O_4 slant column as a function of polynomial order of the high pass filter. If a spectrum in air fit against a nitrogen reference (open red squares) and a helium reference (black diamonds); Panel **(C)**: O_4 slant column error for a spectrum of air + aerosol fit using a nitrogen reference (red squares) and a helium reference (black diamonds).

AMTD
3, 2681–2721, 2010

Inherent calibration of a LED-CE-DOAS instrument

R. Thalman and R. Volkamer

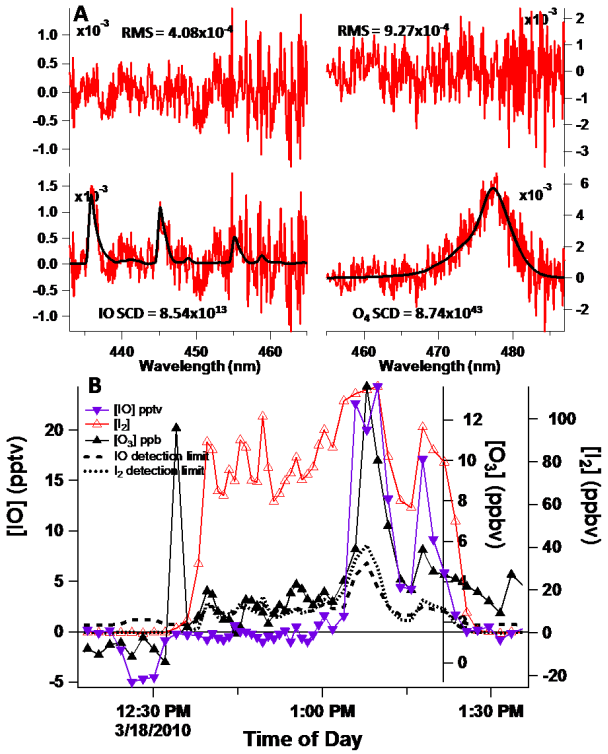

Fig. 7. (A) Example spectrum for the IO detection (4.4 pptv IO, 62 ppbv I_2) (left panel) with the corresponding O_4 fit shown in the right panel. **(B)** Time trace showing the variations in IO, O_3 and I_2, as inferred from the reduction in O_4 path length. The detection limits for IO (dashed line) and I_2 (dotted line) increase towards longer wavelengths because of extinction losses due to I_2 (as seen in part A).

AMTD
3, 2681–2721, 2010

Inherent calibration of a LED-CE-DOAS instrument

R. Thalman and R. Volkamer

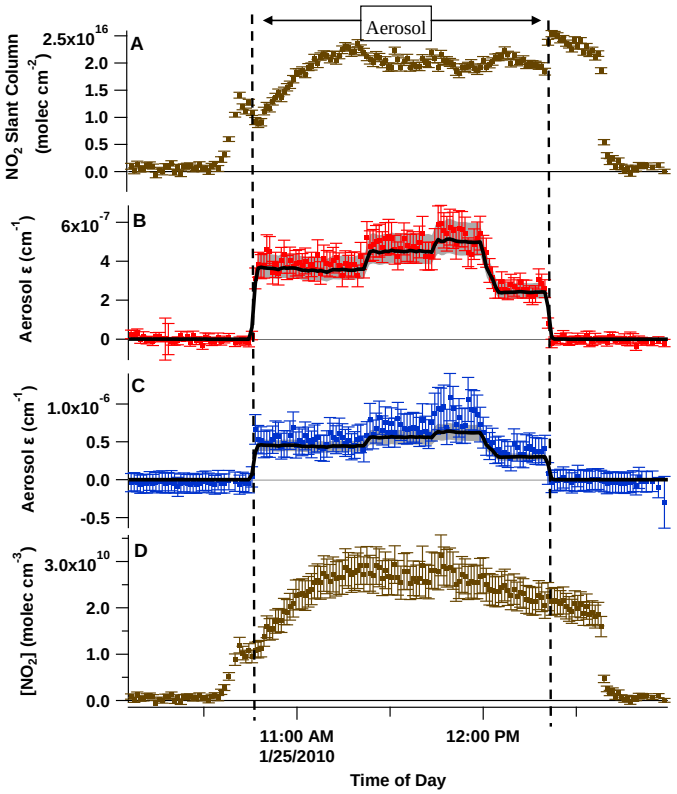

Fig. 8. Simultaneous retrieval of NO_2 and aerosol extinction at two wavelengths in closed cavity mode. **(A)** Retrieved NO_2 slant column density; **(B)** aerosol extinction retrieved from O_4 absorption at 477 nm (red dots) compared to Mie theory (black line, gray area represents uncertainty in size of 350 nm PSLs); **(C)** aerosol extinction retrieved from water absorption at 442.8 nm (blue dots) compared to theory (black line); **(D)** NO_2 concentration corrected for the change in path length measured using O_4.

AMTD
3, 2681–2721, 2010

Inherent calibration of a LED-CE-DOAS instrument

R. Thalman and R. Volkamer

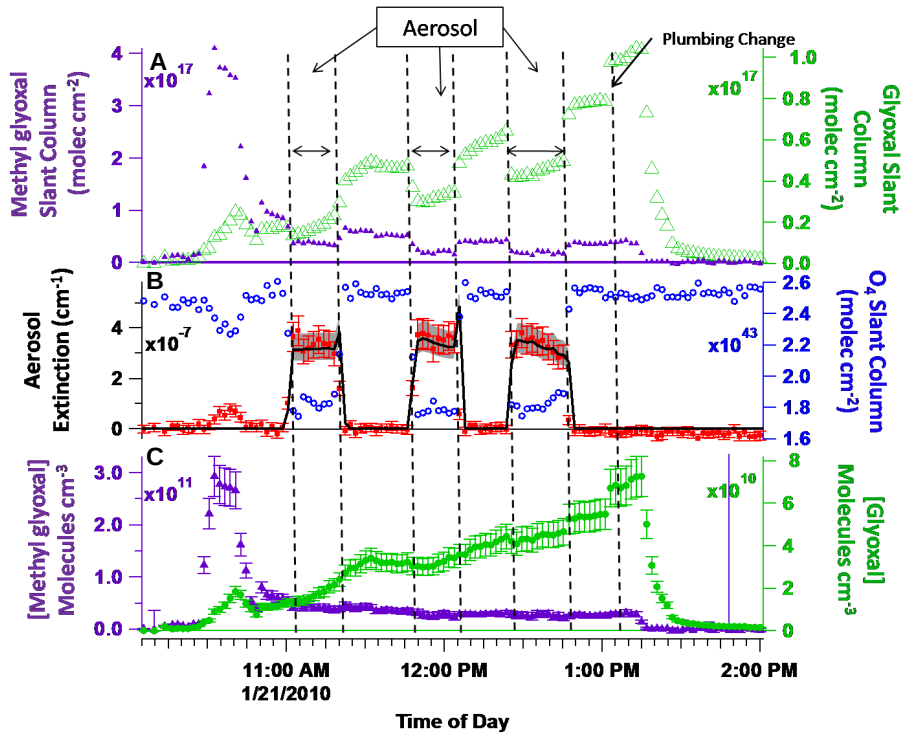

Fig. 9. Simultaneous retrieval of glyoxal, methyl glyoxal and aerosol extinction at one wavelength in closed cavity mode. **(A)**: Slant column densities (SCD) of glyoxal (green open triangles) and methyl glyoxal (purple triangles); **(B)**: O_4 SCD (blue circles), retrieved aerosol extinction from the change in the O_4 SCD (red squares) and the calculated aerosol extinction from Mie theory (solid line, gray area represents the uncertainty in aerosol sizing; peaks at the end of the first two aerosol periods are due to artifacts in the CPC counting); **(C)**: Retrieved concentrations of glyoxal (green dots) and methyl glyoxal (purple triangles) corrected for path length by the retrieved aerosol extinction.

AMTD
3, 2681–2721, 2010

Inherent calibration of a LED-CE-DOAS instrument

R. Thalman and R. Volkamer

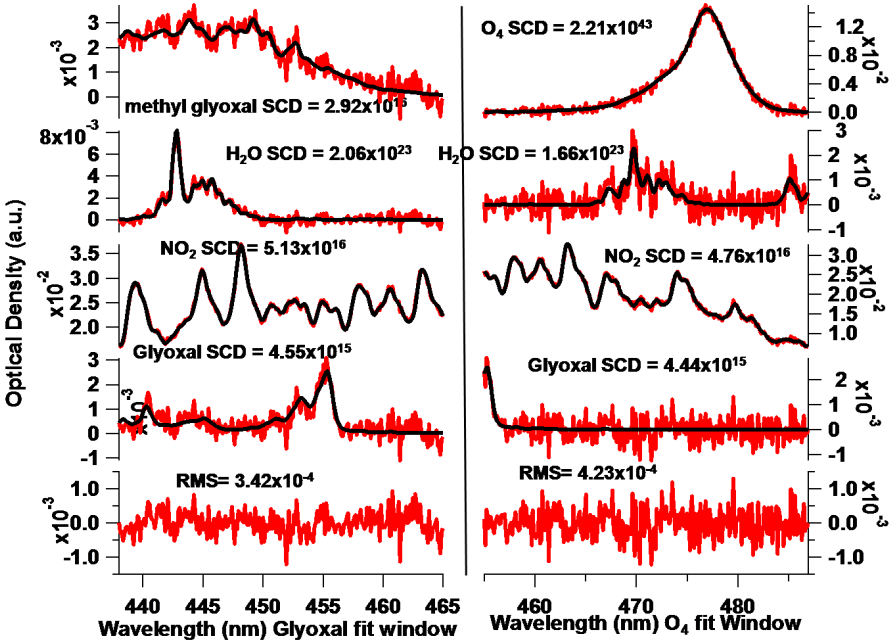

Fig. 10. Example retrievals using LED-CE-DOAS in open cavity mode: glyoxal (274±14 pptv), NO_2 (2.47±0.07 ppbv), methyl glyoxal (1.2±0.2 ppbv), water and O_4.

AMTD
3, 2681–2721, 2010